Journal of Solid State Chemistry 347 (2025) 125338

Contents lists available at ScienceDirect

Journal of Solid State Chemistry

journal homepage: www.elsevier.com/locate/jssc

Effect of sintering temperature on cation distribution in $CoFe_2O_4$ nanoparticles

V. Bilovol [a,*], P. Jeleń [b], K. Mech [a], K. Sokołowski [a], P. Botella [c], E. Bandiello [d], F.J. Manjón [d], D. Errandonea [c]

[a] Academic Centre for Materials and Nanotechnology, AGH University of Krakow, Al. Mickiewicza 30, 30-059, Krakow, Poland
[b] Department of Materials Science and Ceramics, AGH University of Krakow, 32-059, Cracow, Poland
[c] Departamento de Física Aplicada-ICMUV, MALTA Consolider Team, Universitat de València, 46100, Valencia, Spain
[d] Instituto de Diseño para la Fabricación y Producción Automatizada, MALTA Consolider Team, Universitat Politècnica de València, 46022, Valencia, Spain

A B S T R A C T

We report a study of the cation arrangement in $CoFe_2O_4$ nanoparticles synthesized using a co-precipitation method followed by high-temperature sintering in the range of 500–1000 °C. Analysis of the samples by Raman, infrared, and X-ray photoelectron spectroscopy (Fe $2p_{3/2}$ and Co $2p_{3/2}$) revealed that the sintering temperature influences the distribution of cations in the spinel lattice. Specifically, increasing the sintering temperature leads to an increase in the inversion degree parameter (γ), which represents the fraction of Co ions residing in octahedral sites, driving the structure toward a fully inverted spinel. These results are in good agreement with those previously obtained by ^{57}Fe Mössbauer spectroscopy, X-ray diffraction, and X-ray absorption experiments on the same set of samples. Additionally, as shown by the UV–visible spectra, the cationic distribution in the samples clearly affects the band gap value (2.5–2.8 eV).

1. Introduction

$CoFe_2O_4$ (CFO), a spinel-structured oxide, is part of a large family of AB_2O_4 -compounds that include more than eighty different oxides. It has a crystal structure that belongs to the *Fd* $\bar{3}$ *m* space group [1,2]. The cubic spinel structure can be viewed as a cubic close packing of oxygen atoms with Fe and Co cations. The distinguishing feature of this member of the ferrite family is that both Fe^{3+} and Co^{2+} cations are located in the A and B sites, respectively, and both sites have significantly different geometry in terms of their surrounding oxygen atoms. The four oxygen atoms are arranged tetrahedrally around the A position, while the six oxygen atoms are arranged octahedrally around the B position.

The distribution of cations across the two (A and B) sublattices of the spinel structure is strongly influenced by the fabrication method and synthesis conditions. Some of the most widely used methods include chemical co-precipitation [3], high-energy ball milling [4], solid-state reaction [5], hydrothermal synthesis [6], combustion [7], and micro-emulsion [8]. More recent techniques such as spark plasma [9] and flash sintering techniques [10] can also be applicable. The distribution of the cations across the lattice naturally affects the magnetic properties of the ferrimagnetic species. According to the theory of ferrimagnetism proposed by Néel, the net magnetization is due to the unbalanced magnetic moment between the A and B sites, $M = M_B - M_A$, where M_A and M_B are the total sum of all magnetic cations on the A and B sublattices, respectively. Not surprisingly, the magnetic properties of CFO vary according to different configurations of the cations on the two sublattices [11]. Therefore, understanding the cation distribution is critical when designing CFO particles for specific applications. Applications of $CoFe_2O_4$ are numerous and include gas sensors, electronic devices, magnetic recording, medical resonance imaging, to name a few [11]. CFO can also be used as a photocatalyst in water splitting based hydrogen generation or water purification [12–15].

In general, the cationic configuration of cobalt ferrite spinel is described by the following formula: $(Co_{1-\gamma}Fe_\gamma)^A\,[Co_\gamma Fe_{2-\gamma}]^B$, where γ is the degree of inversion of the spinel. A value of $\gamma = 0$ corresponds to a normal spinel with all Co atoms in the tetrahedral A site and $\gamma = 1$ corresponds to an inverse spinel with all Co atoms in the octahedral B site. The degree of inversion is strongly dependent on the synthesis method, and values ranging from 0.20 to 0.96 have been reported in the literature [16–18]. Typically, the degree of inversion is calculated using a limited number of techniques in a given publication, usually one or two [19]. This approach could lead to overestimated or underestimated information, as different techniques have varying sensitivity thresholds. Therefore, it may be beneficial to increase the number of techniques used in a given publication to examine how this parameter is viewed from each technique's perspective. Very rarely, the number of

* Corresponding author.
E-mail address: vbilovol@agh.edu.pl (V. Bilovol).

https://doi.org/10.1016/j.jssc.2025.125338
Received 30 December 2024; Received in revised form 5 March 2025; Accepted 23 March 2025
Available online 24 March 2025

techniques in the analysis of parameter γ exceeds two [20].

One of the most important aspects of any material during its manufacture is the ability to tune its properties by altering the synthesis conditions. $CoFe_2O_4$ exhibits interesting magnetic properties that can be naturally exploited. The magnetic properties of the material discussed in this paper have been previously reported [21]. This paper primarily focuses on analyzing the impact of synthesis conditions on the structural properties of the synthesized materials. We have thoroughly examined the impact of synthesis conditions on the formation of $CoFe_2O_4$ nanoparticles tailored for specific applications that require the highest possible coercive field. We have considered at least two main factors that can significantly affect the final magnetic properties of the synthesized materials: (i) particle size and (ii) the amount of Co on the octahedral site. The first factor (temperature-dependent) is critical for obtaining a system in the single-domain regime, since the multidomain regime leads to a decrease in the coercive field [22]. The second factor has been reported to be responsible for coercivity hardening [23]. On the other hand, as mentioned above, the amount of Co on the octahedral side defines the parameter of the degree of inversion in cobalt ferrite. In a single-domain magnetic regime of nanoparticles along with the maximum value of γ, this should lead to the formation of a $CoFe_2O_4$ nanoparticles with the maximum coercive field.

This work, which continues the previous study by some of the present authors [21], investigates how the temperature factor affects the arrangement of cations in the lattice of ferrimagnetic $CoFe_2O_4$. The material is synthesized through co-precipitation followed by temperature-dependent sintering. Using X-ray diffraction (XRD), transmission ^{57}Fe Mössbauer spectroscopy (MS), and X-ray absorption (XAS) measurements, it was previously shown that the degree of inversion, γ, decreases as sintering temperature decreases for a specific set of $CoFe_2O_4$ nanoparticles [21]. The present study aims to complement the previous one by using a different set of experimental techniques, namely X-ray photoelectron spectroscopy (XPS), Raman scattering spectroscopy (RS), and infrared spectroscopy (IR) measurements, to evaluate their potential in providing results consistent with those previously obtained. The question we seek to answer here is whether the chosen techniques are suitable for estimating the parameter γ.

In this work, we confirm a tendency for Co^{2+} ions to occupy octahedral sites as the sintering temperature increases. Our results based on XPS, RS, and IR measurements are qualitatively consistent with those previously obtained using MS, XRD, and XAS techniques, thereby validating the systematics of our earlier findings. The possible origin of the quantitative discrepancies between all the techniques (the scatter of the results) in the degree of inversion is briefly discussed.

2. Experimental

$CoFe_2O_4$ (CFO) powders were synthesized by the co-precipitation method, the details are given elsewhere [21]. Aqueous solutions of $FeCl_3.6H_2O$ and $CoCl_2.6H_2O$ were used as ferrite precursors. NaOH was used as the precipitation medium. Co-precipitation was performed by slowly dropping the precursor salts into the base solution while stirring. The formed precipitate was centrifuged to pH = 7 and dried at 90 °C. The control of the nanoparticle size was carried out by post-synthesis controlled sintering. The resulting product was divided into fractions, and heat treatments were carried out at 500, 600, 700, 800, 900 and 1000 °C for 5 h in air at a heating rate of 5 °C/min each time for a fresh fraction of powder. It is worth mentioning that after the heat treatment, the natural cooling of the samples took place in the furnace.

The XPS analyses were carried out in a PHI VersaProbeII Scanning XPS system using monochromatic Al Kα (1486.6 eV) X-rays focused to a 100 μm spot and scanned over the area of 400 μm × 400 μm. The photoelectron take-off angle was 45° and the pass energy in the analyzer was set to 46.95 eV (0.1 eV step) to obtain high energy resolution spectra of Co 2p3/2, Fe 2p3/2. A dual beam charge compensation with 7 eV Ar + ions and 1 eV electrons was used to maintain a constant sample surface potential regardless of the sample conductivity. All XPS spectra were charge referenced to the unfunctionalized, saturated carbon (C–C) C1s peak at 285.0 eV. The operating pressure in the analytical chamber was less than 3×10^{-9} mbar. Deconvolution of spectra was carried out using PHI MultiPak software (v.9.9.3). Spectrum background was subtracted using the Shirley method.

Room-temperature unpolarized Raman scattering measurements were performed with a Horiba Jobin Yvon LabRAM HR UV spectrometer equipped with a thermoelectrically cooled multichannel CCD detector. The Raman signal was excited with the 632.8-nm line of a HeNe laser operating at a 10-mW power to avoid sample damage. The use of an ultra-low frequency filter allowed measurements down to 10 cm^{-1}. The spectral resolution was smaller than 2 cm^{-1}.

FT-IR (Fourier Transform Infrared) measurements were performed in the middle (MIR) and far (FIR) infrared range using a Bruker Vertex 70v vacuum spectrometer. MIR measurements were carried out using the standard KBr pellet method. 256 scans in the 4000–400 cm^{-1} were acquired with 2 cm^{-1} resolution. For the FIR measurements, the PE (polyethylene) pellet method was employed. 512 scans, in the 500–100 cm^{-1} range were collected and resolution was set to 2 cm^{-1}. Spectra were subjected to mathematical treatment – cut to specific regions, baseline correction, and normalization using Bruker OPUS 7.2 software.

Diffuse reflectance spectra (DRS) were recorded using a PerkinElmer UV–Vis–NIR Lambda 750 spectrometer equipped with a 100 mm-integrating sphere and an InGaAs detector (PerkinElmer, USA). Spectra were recorded in the wavelength range from 200 to 2400 nm. $BaSO_4$ powder sample was used as a reference. Powder samples were prepared by grinding the mixture containing 15 mg of $CoFe_2O_4$ sintered at different temperatures and $BaSO_4$ (10 wt % of CFO).

3. Results and discussion

Fig. 1 shows a selection of Raman spectra measured in samples prepared by sintering at different temperatures. For each sample, we measured six Raman spectra mapping different parts of the samples. The similar results obtained in different parts of the same sample indicate that our samples were homogeneous. According to group theory, the cubic normal spinel phase has five Raman active modes with symmetries: $\Gamma = A_{1g} + E_g + 3\,T_{1g}$ [21]. These modes are identified in Fig. 2. However, there are two additional modes in the figure that are due to cation inversion [24]. It is known that the highest frequency A_{1g} mode splits into two modes due to cation inversion [24], with the second mode

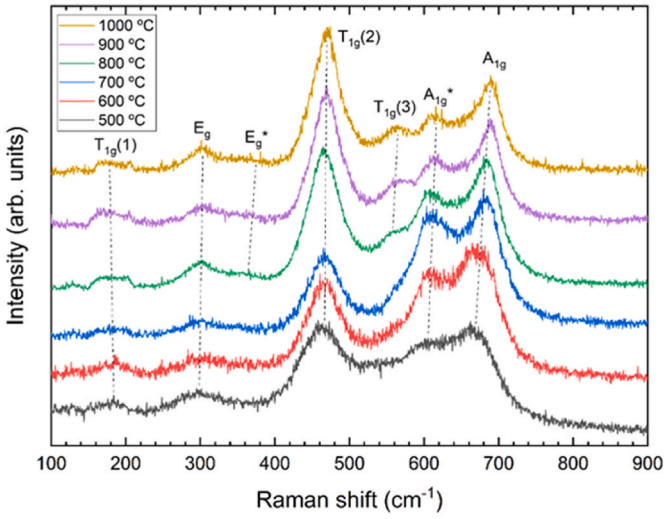

Fig. 1. Room temperature Raman spectra of CFO powders obtained after sintering at different temperatures. The different modes are labelled with their symmetry. Modes at different temperatures are connected by dashed lines.

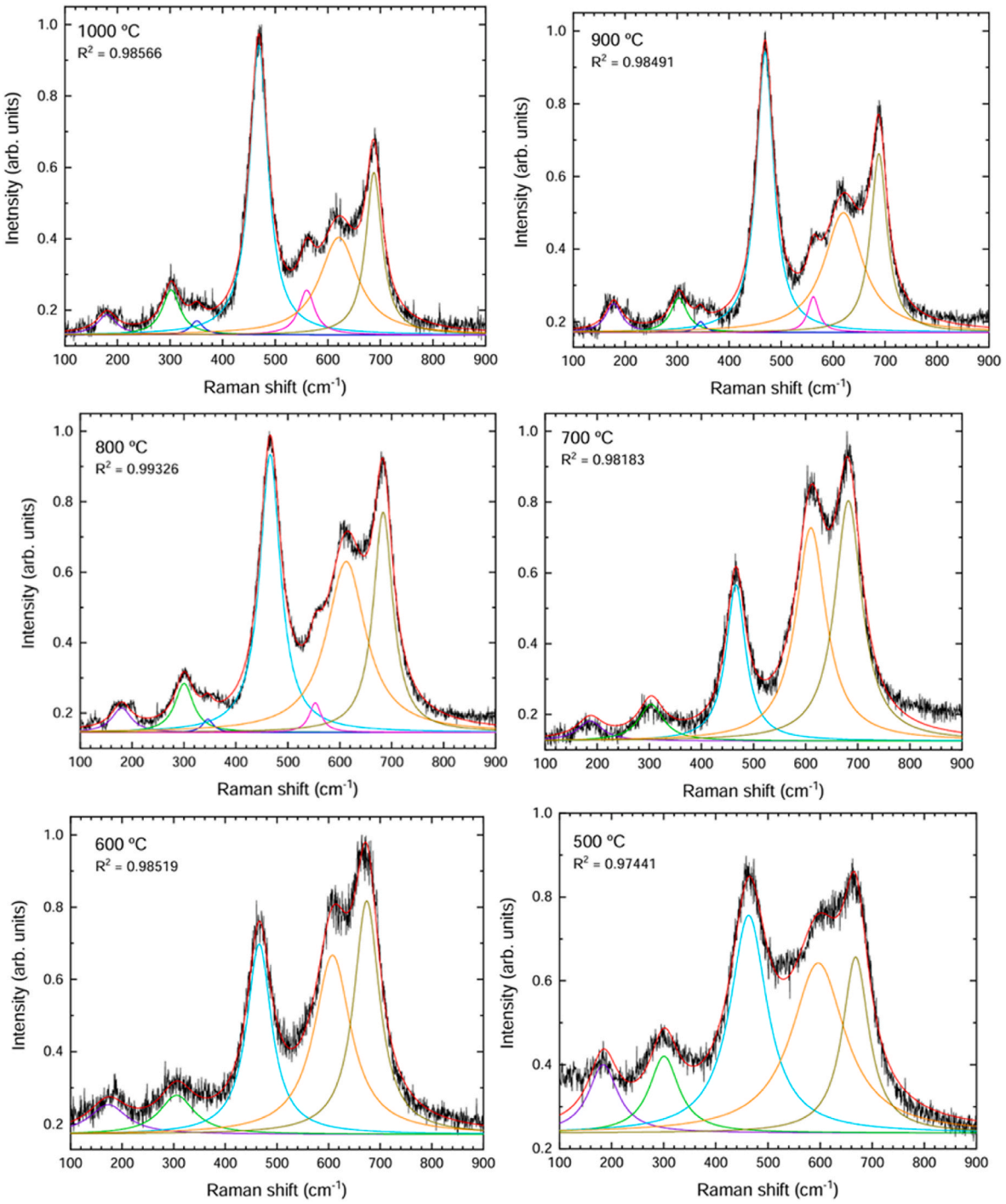

Fig. 2. Raman spectra recorded for samples annealed at different temperatures (indicated in the figure), showing the Lorentzian multipeak fit in red and individual Lorentzian functions in colours. The coefficient of determination R^2 of each fit is given in the plots. All spectra were collected for 120 s. (For interpretation of the references to colour in this figure legend, the reader is referred to the Web version of this article.)

labelled as A_{1g}* in the literature. Both A_{1g} and A_{1g}* modes involve symmetric stretching of oxygen atoms concerning Co and Fe in tetrahedral positions, respectively. We have also observed the splitting of the E_g mode due to cation inversion. In this work, this second mode has been labelled as E_g*. Both E_g and E_g* modes correspond to a symmetric bending motion of the oxygen anions concerning Co and Fe ions within tetrahedral units. Therefore, the splitting of both A_g and E_g modes supports cation inversion. The more intense the A_{1g}* and E_g* modes compared to A_{1g} and E_g, the higher the degree of cation inversion, i.e. the higher the value of the γ parameter. As for the rest of the Raman modes, the $T_{1g}(2)$ and $T_{1g}(3)$ modes correspond to the vibrations of the octahedral group. $T_{1g}(2)$ is associated with asymmetric stretching vibrations and $T_{1g}(3)$ is due to asymmetric bending vibrations of oxygen atoms [25]. Finally, the lowest frequency mode $T_{1g}(1)$ is related to a translational motion of the whole tetrahedron as a rigid mode [25].

It can be seen in Fig. 1 that the peaks become broader as the sintering temperature decreases, which is a consequence of the decrease in the particle size [17]. The change in peak width is caused by the inhomogeneous strain broadening associated with the reduction of particle size and by phonon confinement [26,27]. Due to the phonon broadening

only five peaks can be distinguished in the samples thermally treated at 500, 600, and 700 °C. At these temperatures, the E_g* and $T_{1g}(1)$ modes are barely distinguishable. The disappearance of the E_g* mode with decreasing sintering temperature suggests less cation inversion at lower sintering temperatures. This conclusion is also supported by a systematic comparison of the areas under peaks A_{1g}* and A_{1g}, which we will present after reporting a multipeak fit analysis of the Raman spectra.

Fig. 1 also shows that, except for the lowest frequency $T_{1g}(1)$ mode, all Raman modes shift to higher frequencies with increasing particle size (increasing sintering temperature). Thus, the sintering temperature in $CoFe_2O_4$ plays a role analogous to that of hydrostatic compression. This phenomenon has been observed in other nanoparticles, where reducing the particle size (reducing the sintering temperature in our study) induces a negative pressure in the nanoparticles [28]. As mentioned above, the lowest frequency mode $T_{1g}(1)$ follows an opposite behaviour to the other modes, as also observed in high-pressure experiments. The frequency of this mode decreases slightly with increasing sintering temperature (see Fig. 1). As described above, the $T_{1g}(1)$ mode is related to a rigid translation of the tetrahedra, indicating that the tetrahedral units are distorted as the particle size decreases. Such a decrease in the frequency of a translational mode has been observed in other oxides [29] and is associated with the existence of phase transitions. The behaviour of the $T_{1g}(1)$ mode seems to indicate that, probably by applying a sintering temperature higher than 1000 °C, but lower than the melting temperature (1570 °C) [30] $CoFe_2O_4$ nanoparticles could crystallize in the tetragonal spinel structure of this compound [31].

To perform a quantitative analysis of the Raman spectra, we have performed a Lorentzian multipeak analysis (see the results of the fits in Fig. 2 and Table 1). The fitting procedure was performed using Origin software. Lorentzian functions are characterized by peak intensity, peak centre position, and peak width, which is half of the full width at half maximum. The three parameters for each Lorentzian function were taken as fitting parameters, so that a total of 21(15) parameters were used in the fits for samples sintered at 800, 900, and 1000 °C (500, 600, and 700 °C), with no restriction on peak width. The initial values of the fitting parameters were determined manually using the Peak Analyzer tool of the software used. The Raman spectra were then fitted iteratively until the total residuals were minimized and no further improvements could be achieved. The frequencies in Table 1 confirm that the phonon frequency of the $T_{1g}(1)$ mode decreases with increasing sintering temperature and that the opposite behavior is observed for the other modes. The peak widths in Table 1 confirm the broadening of the peaks with decreasing sintering temperature. Finally, the intensity and peak width information in Table 1 allows us to calculate the area under the peaks, which will be used later to analyze the cation inversion after comparing the phonon frequencies with previous studies. It should be noted that the A1g* peak is much broader than the other peaks (see Fig. 2 and the FWHM in Table 1) and that the weakness of the peak increases with increasing sintering temperature. This is related to the fact that the presence of this peak is a consequence of cationic inversion, which we have found to increase with increasing sintering temperature. Cationic inversion could cause a local disorder of the crystal structure, which would broaden the peaks of the associated Raman modes, as observed here.

In Table 2, we compare the Raman frequencies determined in this work with those previously reported in the literature [24,32,33]. The frequencies of all modes, except for the $T_{1g}(1)$ mode, are slightly smaller than in bulk $CoFe_2O_4$ [32] and agree well with a previous study on 10–20 nm nanoparticles of $CoFe_2O_4$ [24]. On the other hand, the frequency of the $T_{1g}(1)$ mode is 20 cm^{-1} smaller than in Refs. 16 and 28. The reason could be related to the different synthesis methods or the use of different laser excitation lines [34]. A detailed analysis of this difference is beyond the scope of this study. It is noteworthy that the frequency we measured for the $T_{1g}(1)$ mode is similar to that reported in Ref. 30 for $CoFe_2O_4$ nanoparticles of unknown particle size. The frequencies of the remaining modes reported in that study [32] are more similar to the frequencies we determined for the sample with a sintering temperature of 500 °C.

As mentioned above, the frequencies reported in Table 2 are important for estimating the degree of cation inversion. In this sense, it is important to explain why the A_{1g} mode is assigned to CoO_4 tetrahedral units and the A_{1g}* mode is assigned to FeO_4 tetrahedral units. This mode assignment is not based only on previous studies [24] but also on the different frequencies of the A_{1g} mode in spinel Co_3O_4 (690 cm^{-1}) [35] and in spinel Fe_3O_4 (640 cm^{-1}) [36]. Therefore, it is quite reasonable that in $(Co_{1-x}Fe_x)(Fe_{2-x}Co_x)O_4$ spinel, the A_{1g} mode is split into a higher

Table 1
Information obtained from the multipeak fit of Raman spectra measured in CFO powders. The frequency (ω) and full with at half maximum (w) of each mode are reported, along with the area under the peak associated with each mode.

Mode	$T_{1g}(1)$	E_g	E_g*	$T_{1g}(2)$	$T_{1g}(3)$	A_{1g}*	A_{1g}
Sintering temperature 1000 °C							
ω (cm^{-1})	177(1)	304.3(8)	351(2)	468.9(1)	559.9(7)	620.8(8)	689.6(2)
w (cm^{-1})	43(5)	41(3)	29(7)	42.7(3)	36(3)	88(4)	37.6(9)
A (a.u.)	3.8(3)	8.2(4)	1.8(4)	54.5(4)	7.1(1)	43(2)	24.8(8)
Sintering temperature 900 °C							
ω (cm^{-1})	178(1)	304(1)	347(2)	469(1)	562(7)	619.9(7)	688.2(2)
w (cm^{-1})	38(4)	38(3)	20(7)	40.2(4)	26(3)	90(3)	38.2(8)
A (a.u.)	4.7(4)	5.7(4)	1.0(3)	48.7(4)	3.9(6)	47.2(9)	29.2(8)
Sintering temperature 800 °C							
ω (cm^{-1})	180(1)	303.5(6)	344(2)	466.0(1)	552.9(8)	612.5(4)	683.5(2)
w (cm^{-1})	45(4)	43(2)	25(6)	48 (3)	28(4)	91(2)	45.9(6)
A (a.u.)	5.0(3)	9.4(4)	1.5(3)	59.8(4)	3.7(6)	69(2)	45.1(8)
Sintering temperature 700 °C							
ω (cm^{-1})	182(3)	303(3)		466.0(3)		610.0(4)	681.9(4)
w (cm^{-1})	58(4)	58(4)		45.3(9)		71(1)	63(1)
A (a. u.)	6.2(9)	10.4(8)		31.5(5)		68(1)	60(1)
Sintering temperature 600 °C							
ω (cm^{-1})	183(2)	302(1)		465.7(2)		607.8(6)	674.0(3)
w (cm^{-1})	89(8)	82(6)		58.0(9)		86(2)	60(1)
A (a.u.)	11.4(9)	13.8(9)		47.9(6)		67(2)	62(1)
Sintering temperature 500 °C							
ω (cm^{-1})	184(3)	300(2)		463.0(4)		597(2)	668.3(5)
w (cm^{-1})	88(9)	78(9)		86(1)		125(5)	61(2)
A (a.u.)	17.5(5)	19.8(4)		70(1)		74(5)	69(3)

Table 2
Comparison of our Raman frequencies (in cm^{-1}) in CFO powders with those of previous studies ([a]Ref. 32, [b]Ref. 17, and [c]Ref. 31). The sintering temperatures are given in the table.

Mode	Bulk[a]	10-20 nm[b]	Nano[c]	This work					
				1000 °C	900 °C	800 °C	700 °C	600 °C	500 °C
$T_{1g}(1)$	210	205(1)	174–183	177(1)	178(1)	180(1)	182(3)	183(2)	184(3)
E_g	312	309(1)	293–297	304.3(8)	304(1)	303.5(6)	303(3)	302(1)	300(2)
E_g*				351(2)	347(2)	344(2)			
$T_{1g}(2)$	470	468(1)	458–462	468.9(1)	469(1)	466.0(1)	466.0(3)	465.7(2)	463.0(4)
$T_{1g}(3)$	575	563(1)	526–539	559.9(7)	562(7)	552.9(8)			
A_{1g}*	624	613(1)	595–601	620.8(8)	619.9(7)	612.5(4)	610.0(4)	607.8(6)	597(2)
A_{1g}	695	688(1)	671–677	689.6(2)	688.2(2)	683.5(2)	681.9(4)	674.0(3)	668.3(5)

frequency A_{1g} mode associated with the stretching vibrations of the CoO_4 tetrahedron and a lower frequency A_{1g}* mode associated with the stretching vibrations of the FeO_4 tetrahedron.

We will now use the results reported in Table 1 to obtain information about the cation inversion in our samples. The table shows that the area of the E_g* peak is greater than zero only at sintering temperatures of 800, 900, and 1000 °C. This indicates an increase in the Fe content in the tetrahedral sites, i.e. an increase in the cation inversion with a consequent increase in the occupation of the octahedral sites by Co atoms. From the areas (A) under the A_{1g} and A_{1g}* peaks the degree of cation inversion can be estimated as $\gamma = A_{A1g^*}/(A_{A1g} + A_{A1g^*})$ [24]. The results are shown in Fig. 3, where they are compared with results obtained previously from XRD and Mössbauer spectroscopy [21] and in this study from XPS measurements (for selected samples). The four techniques show a qualitatively similar trend. According to Raman measurements, γ increases from 0.51 for a sintering temperature of 500 °C to 0.64 for a sintering temperature of 1000 °C.

In addition to the Raman study, we performed another vibrational analysis using IR spectroscopy. The $CoFe_2O_4$ spinel belongs to the T_d point group and has four infrared active modes with symmetry T_{1u}, which are usually observed as bands labelled ν_1-ν_4 (see Fig. 4). The bands are broader than the Raman modes due to the LO-TO splitting. The IR band with the highest wavenumber, ν_1, at about 600–500 cm^{-1}, is predominantly related to stretching vibrations of the tetrahedra, and the ν_2 band, at 400–300 cm^{-1}, is predominantly related to stretching vibrations of the octahedra. On the other hand, the modes with lower

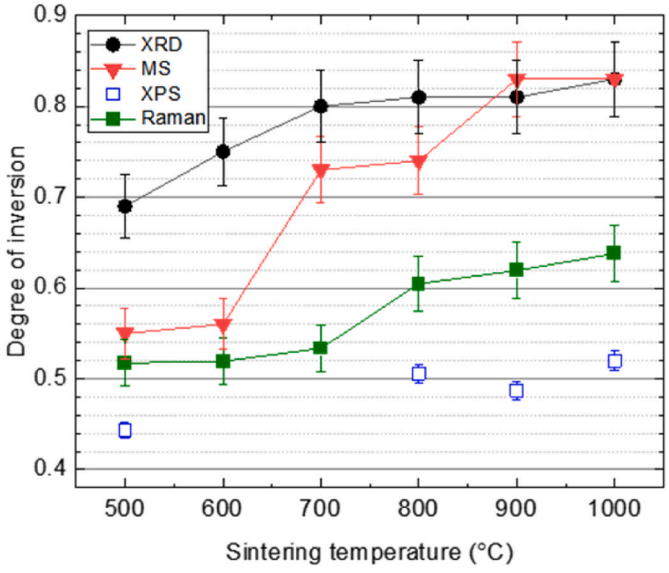

Fig. 3. Parameter γ (degree of cation inversion) versus sintering temperature as determined by XPS (selected samples) and Raman (RS) measurements. The results of XRD and Mössbauer (MS) spectroscopy measurements reported in Ref. 21 for the same samples are also shown for comparison.

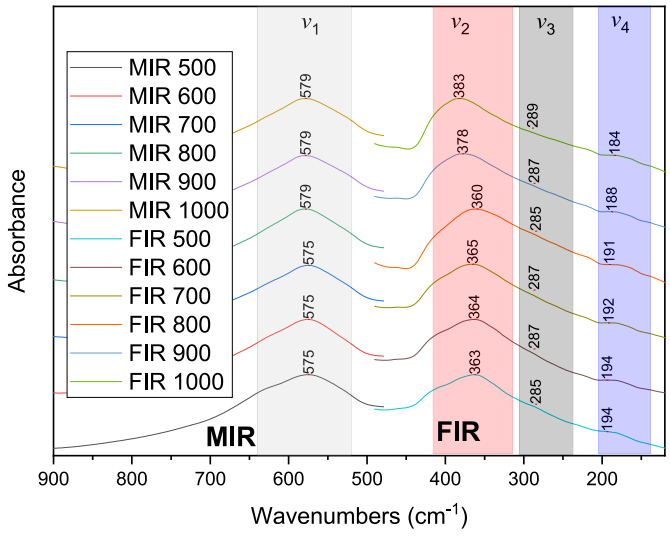

Fig. 4. MIR and FIR spectra of cobalt ferrites.

wavenumbers are more complex vibrations, involving both octahedra and tetrahedra. The ν_3, which appears as a shoulder of ν_2, can be attributed to the interactions of metals in tetrahedral and octahedral sites [37–42]. Band wavenumbers and assignments of the different IR bands are shown in Table 3 and Fig. 4.

As can be seen in Fig. 4, the IR spectrum of cobalt ferrite obtained after sintering at 500 °C, shows the typical vibrations of cubic ferrites. The strong ν_1 band at 575 cm^{-1} has a significant shoulder at higher wavenumbers (about 650 cm^{-1}) and is a typical broadening characteristic of a disordered structure [37,40]. This indicates that the spinel structure of our CFO powders is disordered. With increasing temperature, the shoulder disappears and there is a slight shift of this band towards the higher wavenumbers, from 575 to 579 cm^{-1}. The disappearance of the shoulder is probably due to better crystallization of the sample with increasing temperature and the wavenumber shift is probably due to the change in B-site occupancy, as discussed below. The most significant shift is observed in the ν_2 band. It moves from 363 to 383 cm^{-1} as the sintering temperature is increased. To understand this

Table 3
Wavenumbers of the four IR bands in CFO powders annealed at different temperatures.

Temperature (°C)	Wavenumber (cm^{-1})			
	ν_1	ν_2	ν_3	ν_4
500	575(1)	363(1)	285(1)	194(1)
600	575(1)	364(1)	287(1)	194(1)
700	575(1)	365(1)	287(1)	192(1)
800	579(1)	360(1)	285(1)	191(1)
900	579(1)	378(1)	287(1)	188(1)
1000	579(1)	383(1)	289(1)	184(1)

phenomenon, it is necessary to calculate the "covalency"/bond strength of the Co–O and Fe–O bonds in the spinel structure in octahedral positions [43,44]. From the N–V parameter (N – number of unpaired electrons, V – valence state) it is possible to assess the degree of spinel inversion. The higher the parameter, the lower the covalency and therefore the lower the bond strength. This in turn implies a shift towards lower wavenumbers. The calculations for octahedral cations are as follows: Co^{2+}: 3-2 = 1, while Fe^{3+}: 5-3 = 2 [43,44]. Therefore, an increase in the Co occupation of the octahedral sites will lead to an increase in IR phonon wavenumbers. The results for the ν_2 modes (see Fig. 5) show a shift towards higher wavenumbers, implying that the octahedral sites become occupied by cobalt ions as the sintering temperature increases. This is further evidenced by the slight shift of the ν_3 vibration to higher wavenumbers, which is additionally attributed to the interaction of metals in tetra- and octahedral sites, confirming the ongoing changes. The opposite behaviour is observed in the ν_4 band. With increasing temperature, the vibration of interacting metals in tetrahedral configuration shifts this band to lower wavenumbers. Finally, the mode v3 is essentially unaffected by the sintering temperature. This is not surprising since this mode is related to the interaction between cations, which is not much affected by cation inversion. In summary, the ν_2 band can be considered as an indicator of the degree of inversion in spinels. Its position is directly related to the presence of cobalt in the octahedral positions. As the temperature increases, it is clearly visible that the position of this band begins to shift, at first slightly, and then more significantly. Thus, IR spectroscopy qualitatively confirms the trend obtained more quantitatively by RS spectroscopy.

It should be noted that the analysis of XPS measurements is a very powerful technique to quantitatively determine the chemical composition at the atomic level down to about 5 nm from a surface. The peak position (binding energy) identifies the element, while the peak intensity is proportional to the amount of the element in the sample. The surface concentrations of chemical bonds obtained by fitting XPS data for the samples (from their survey spectra) are listed in Table 4. The presence of Na, C and trace amounts of Ca and Pb on the surface is a consequence of the synthesis route and environmental conditions and does not affect the magnetic properties of the particles. Additionally, it does not influence the Co/Fe ratio in the studied region. Figs. 6 and 7 show the XPS spectra of the $Co2p_{3/2}$ $Fe2p_{3/2}$ levels in the (selected) CFO samples. The detailed cationic distribution of the ions was quantitatively estimated by calculating the deconvolution of the peak area corresponding to the octahedral and tetrahedral geometries of the cobalt ions. We discard the existence of Co^{3+} ions in our samples, otherwise it would imply the existence of Fe^{2+} ions due to the charge balance. The latter was discarded by the Mössbauer spectroscopy (MS) measurements in our previous studies [21]. With increasing sintering temperature, the Co^{2+} ions tend to occupy the octahedral sites, i.e. the inversion degree parameter γ increases. This trend is opposite to that reported by Liu et al. [45] who studied the cation distribution in $CoFe_2O_4$ nanofibers annealed in the range of 700–850 °C. However, it is consistent with our Raman trend discussed above, as well as the XRD and Mössbauer spectroscopy results supported by XAS.

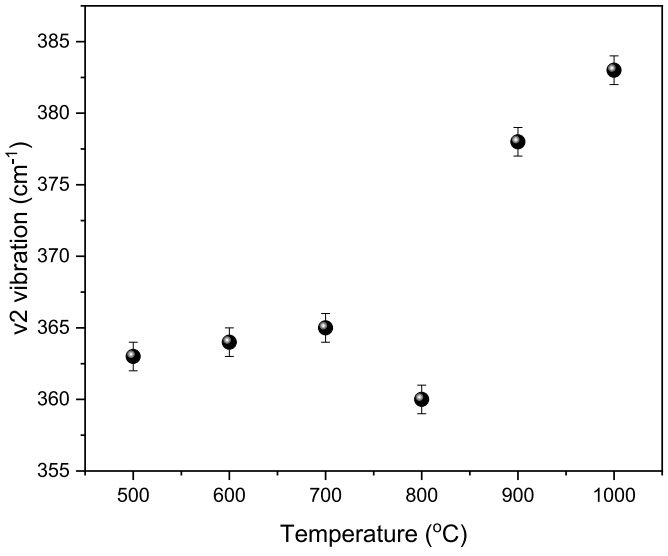

Fig. 5. Wavenumber of the IR ν_2 vibration versus sintering temperature.

The Fe $2p_{3/2}$ spectra (Fig. 6) are similar for all samples where iron was detected. Each spectrum was fitted with up to six lines, with the first found at 709.5 eV, indicating the presence of the Fe^{3+} oxidation state as in Fe_2O_3. Four lines in the 710–715 eV energy range are due to the multiplet splitting phenomena. The broadening and shifted shake-up energy up to 718.2 eV is a characteristic behaviour for Fe^{3+}, providing additional evidence for Fe^{3+} species in the samples [50,51].

The Co $2p_{3/2}$ region for the samples (Fig. 7) was fitted with five components. The first and third lines at 778.8 eV and 781.4 eV represent the main photoemission line of the Co^{2+} octahedral site and the multiplet splitting (ms) component of the Co^{2+} octahedral site as in Co_3O_4 species. The second and fourth lines at 779.9 eV and 782.9 eV are the pair components (main and ms) attributed to the Co^{2+} cations in the octahedral sites, as in CoO species. The last broadening line at 785.6 eV is the shake-up satellite component associated with the Co^{2+} cations, corresponding to a high spin-orbital state (S = 3/2) of Co^{2+} [50,52]. Using the quantitative results of the deconvoluted spectra, the parameter of the degree of inversion was calculated for each sample, as shown in Fig. 3.

Diffuse reflectance spectra (Fig. 8) were measured to investigate the band gap of $CoFe_2O_4$ nanoparticles by UV–visible diffuse reflectance spectroscopy. To identify the band gap energies of all the CFO samples, $[F(R)E]^2$ is plotted against $h\nu$, where F(R) is the Kubelka-Munk function $F(R) = (1-R)^2/2R$, where R is the reflectance in UV–Vis spectra. By extrapolating $[F(R)E]^2$ to zero, as shown in Fig. 8, the value of the direct band gap energy was estimated. The value of the band gap energy obtained by this method may slightly underestimate the energy of the fundamental band gap [53]; however, the offset of the band gap energy is the same for all samples, allowing for a systematic comparison between samples (same reference as above). The obtained results (2.5–2.8 eV) are consistent with those reported by other researchers [54–57] and show a clear trend: the value of the band gap energy increases with increasing particle annealing temperature. Srinivas [57] reported the dependence of the band gap energy on the cation distribution in Ni-doped cobalt ferrite. The reported trend is similar to what we observe in our CFO samples: the greater the occupancy of the octahedral sites by Co ions, the greater the observed value of the band gap energy. This dependence was attributed to the different interatomic distances between the anion and cations due to the size differences of the cations in tetrahedral and octahedral positions. Sharma and Khare reported the relationship between Co^{2+} distribution among the tetrahedral-octahedral positions and the optical band gap energy in $CoFe_2O_4$ thin films annealed at different temperatures [58]. The authors observed the opposite effect of the annealing temperature on the band gap position, manifested by the decrease of the band gap energy with the increase of the annealing temperature. It should be noted that the authors reported that the direct band gap was located at significantly lower energies compared to the results reported in this work. Holinsworth et al. reported that the direct band gap in $CoFe_2O_4$ has an energy of about 2.7 eV, which is in good agreement with our data, while the indirect band gap is located at an energy close to 1.2 eV [59].

In summary, qualitatively, all the techniques show the same trend; however, quantitatively, there is a discrepancy between the results obtained by the techniques applied.

Therefore, it is useful to mention the reasons that could lead to these quantitative discrepancies. XRD is a technique based on the diffraction of electrons. Elements with a similar number of electrons, when adjacent

Table 4
Surface composition (atomic %) of the samples determined by survey XPS measurements. The assignment of chemical bonds was done on the basis of references [46–49].

Element	C			O			Na	Ca	Fe	Co			Pb
Energy [eV]	285.0	286.6	288.8	529.7	531.4	532.9	1071.5	347.1	709.5	778.8	780.1	785.6	138.2
Groups/Ox.state	C–C	C–*O*–C, C–OH	C═O	O–Me(latt.)	O–Me(def.) O═C	O–C, OH, H_2O ads.	Na^+	Ca^{2+}	Fe^{3+}	Co^{2+} (O_h)	Co^{2+} (T_d)	Sat. (Co^{2+})	Pb^{2+}
500	11.2	4.1	2.5	33.2	11.8	2.6	0.8	0.2	20.6	2.7	3.4	6.7	0.1
800	10.1	2.0	1.7	35.2	9.5	2.2	5.0	0.7	18.7	3.9	3.8	7.0	0.2
900	10.3	1.9	1.2	36.5	9.7	2.5	3.4	1.3	19.1	3.7	3.9	6.3	0.3
1000	10.2	2.5	1.7	36.3	11.2	3.6	0.7	2.3	17.1	4.0	3.7	6.5	0.2

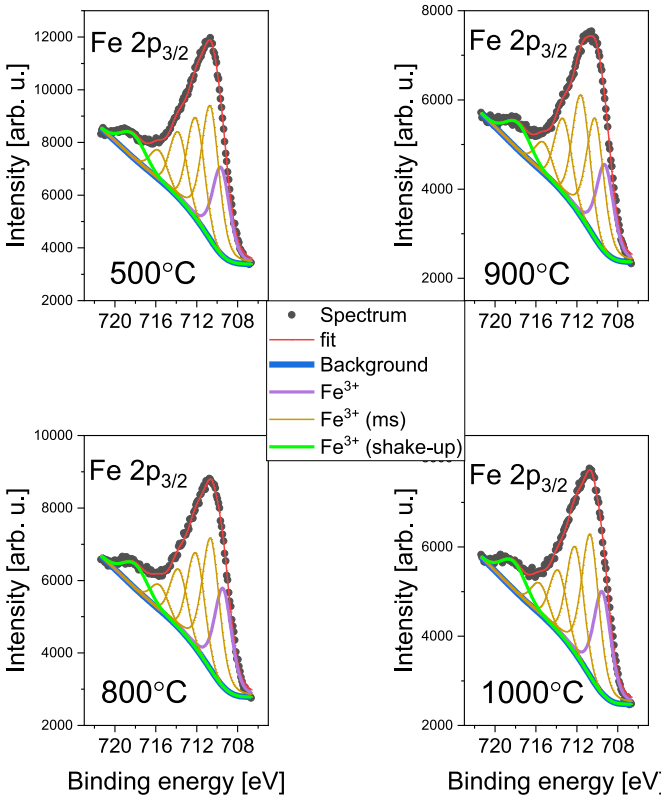

Fig. 6. Fe $2p_{3/2}$ core-level XPS spectra for (selected) CFO samples annealed at different temperatures.

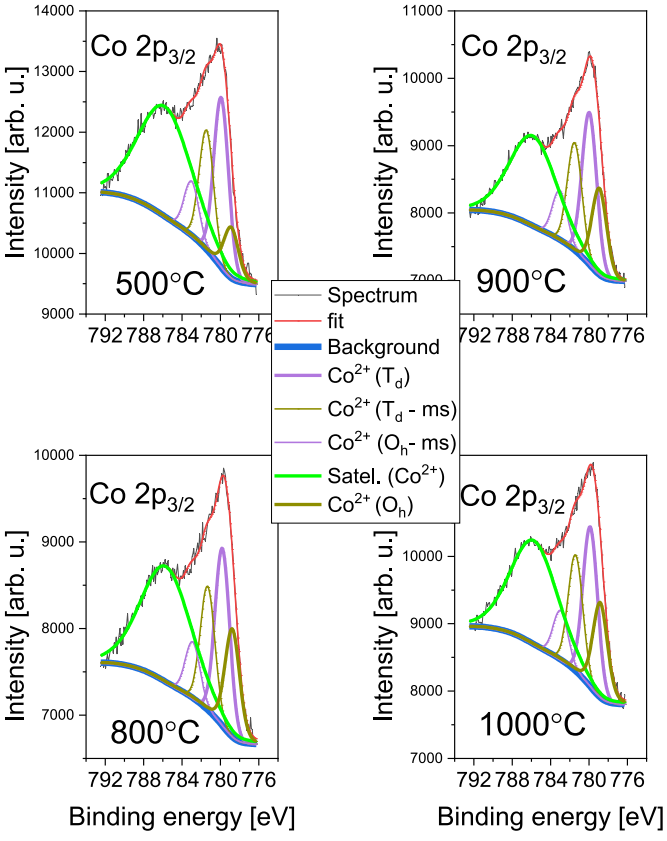

Fig. 7. Co $2p_{3/2}$ core-level XPS spectra for (selected) CFO samples annealed at different temperatures.

in the periodic table, have similar scattering factors. In the case of conventional XRD, obtaining an accurate cation occupancy can be a challenge. XPS is a surface-sensitive technique, meaning that the chemical state of the surface can be different from that of deeper states. Therefore, XPS cannot provide complete information about the chemical state of the particles as a whole.

In the case of MS, this technique is extremely sensitive to the atomic probe (Fe in our case). If the model used to fit the Mössbauer spectra is properly chosen, the estimation of the degree of inversion can be very accurate and, therefore, reliable.

As for RS, if we assume that the oscillations of the phonons are harmonic, the frequency is in principle $\sqrt{k/m}$, where k is the force constant and m is the mass of the atom. Consequently, for two atoms, that are neighbours in the periodic table, RS is probably not the most sensitive way to determine the degree of inversion, especially in nanomaterials.

4. Conclusions

A series of $CoFe_2O_4$ nanoparticles synthesized through co-precipitation followed by temperature-dependent sintering in the range of 500–1000 °C has been analyzed using Raman, IR and XPS techniques to track the degree of spinel inversion, defined as the amount of Co^{2+} ions in the octahedral sites. The results obtained from vibrational techniques (Raman and infrared spectroscopy) are qualitatively consistent, suggesting that Co ions prefer to occupy the octahedral sites as the sintering temperature increases. The same trend was observed using X-ray photoelectron spectroscopy. The different distribution of Co^{2+} ions in the CFO samples with varying sintering temperatures is also reflected in changes to the optical band gap. It provides opportunities for tuning the band structure with respect to the use of synthesized and thermally treated CFO in photocatalytic water splitting or water purification processes. All these results align with those previously obtained using ^{57}Fe Mössbauer spectroscopy, X-ray diffraction, and X-ray absorption measurements. This allows us to conclude with certainty that the temperature factor affects the distribution of ions in cobalt ferrite particles: higher temperatures favor the occupancy of the octahedral sites by Co^{2+} ions, i.e. CFO spinels tend to become fully inverse spinels as sintering temperature increases. Although all the techniques involved in the investigation show the same trend, the quantitative results for

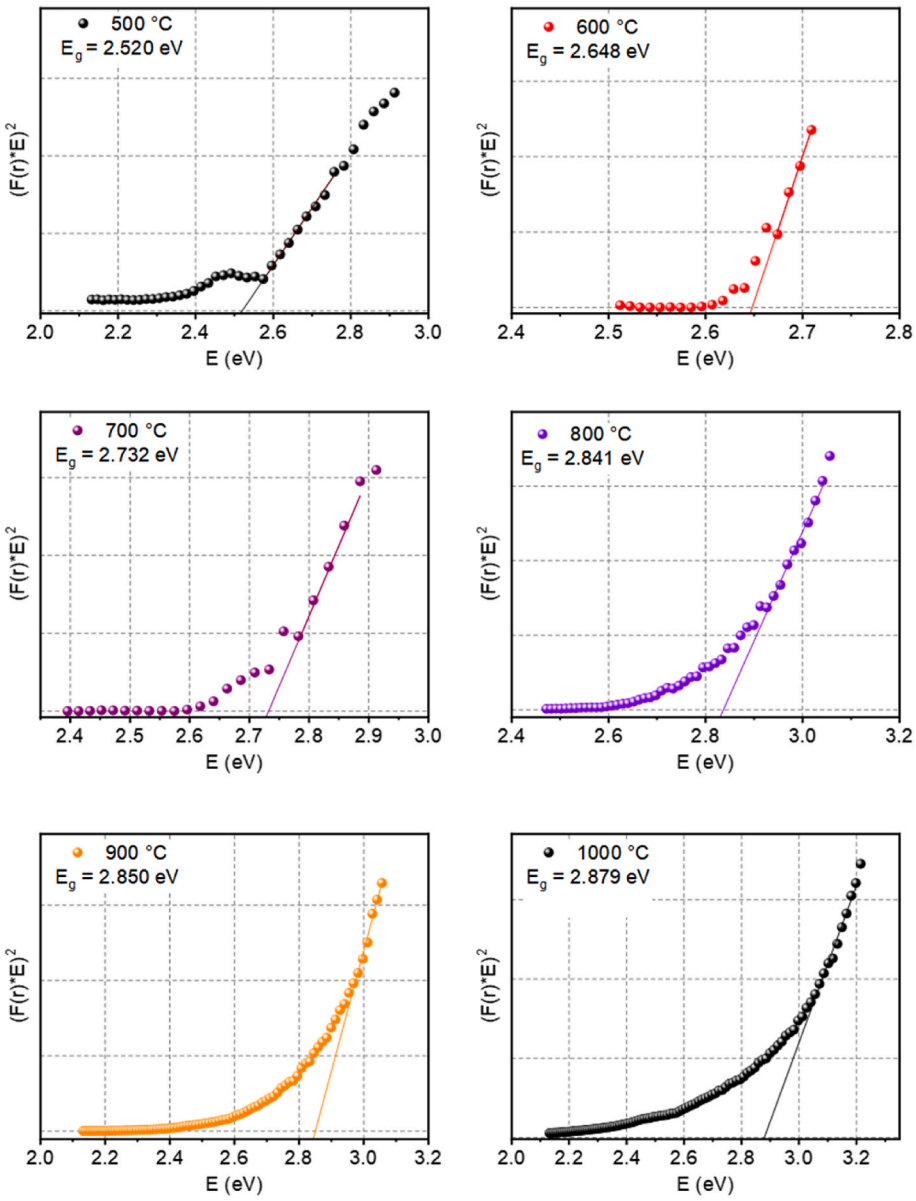

Fig. 8. UV–visible diffuse reflectance spectra. The point where the straight line intersects the energy axis is taken as the direct band gap.

defining the inversion degree parameter (γ) differ somewhat due to the varying sensitivities of the techniques involved. It can be concluded that, for a more accurate estimation of γ in cases when it truly matters, the use of more than one technique is highly recommended. Among the techniques discussed in this study, ^{57}Fe Mössbauer spectroscopy appears to provide the most reliable results, at least for the Fe-containing samples.

CRediT authorship contribution statement

V. Bilovol: Writing – review & editing, Writing – original draft, Visualization, Validation, Supervision, Project administration, Investigation, Formal analysis, Conceptualization. **P. Jeleń:** Writing – original draft, Investigation, Data curation. **K. Mech:** Writing – review & editing, Writing – original draft, Investigation, Data curation. **K. Sokołowski:** Writing – original draft, Software, Investigation, Data curation. **P. Botella:** Investigation, Data curation. **E. Bandiello:** Investigation, Data curation. **F.J. Manjón:** Writing – original draft, Investigation, Data curation. **D. Errandonea:** Writing – original draft, Investigation, Data curation.

Declaration of competing interest

The authors declare that they have no known competing financial interests or personal relationships that could have appeared to influence the work reported in this paper.

Acknowledgements

This research was partly supported by the program "Excellence Initiative - Research University" for the AGH University of Krakow. This publication is financed by the Spanish Ministerio de Ciencia, Innovación y Universidades (MCIU) and the Agencia Estatal de Investigación (AEI) (https://doi.org/10.13039/501100011033) as part of the project MALTA Consolider Team network (RED2022-134388-T), and I + D + i projects PID2022-138076NB-C41/C42 co-financed by EU FEDER funds. This publication is also financed by Generalitat Valenciana through grants PROMETEO CIPROM/2021/075-GREENMAT, MFA/2022/007, and MFA/2022/025 (ARCANGEL). This study forms part of the Advanced Materials program and is supported by MCIN with funding from the European Union Next Generation EU (PRTR-C17.I1) and by the

Generalitat Valenciana. We thank Dr. M. Marzec and. Dr. D. Lachowicz for their help with the XPS and optical measurements, respectively. V.B. is thankful to the Polish National Agency for Academic Exchange (NAWA) for the fellowship (BPN/ULM/2021/1/00076).

Data availability

Data will be made available on request.

References

[1] R.J. Hill, J.R. Craig, G.V. Gibbs, Phys. Chem. Miner. 4 (1979) 317–339, https://doi.org/10.1007/BF00307535.
[2] D. Errandonea, AB_2O_4 compounds at high pressures, in: F.J. Manjón, I. Tiginyanu, V. Ursaki (Eds.), Pressure-Induced Phase Transitions in AB_2X_4 Chalcogenide Compounds, vol. 189, Springer Series in Materials Science, Berlin, Heidelberg, 2014, https://doi.org/10.1007/978-3-642-40367-5. Springer.
[3] V. Bilovol, J. Zukrowski, M. Sikora, D. Errandonea, K. Berent, M. Gajewska, Effect of sintering temperature on structural, elastic, and hyperfine features, Effect of sintering temperature on structural, elastic, and hyperfine features of nickel ferrite nanoparticles of nickel ferrite nanoparticles, J. Magn. Magn Mater. 591 (2024) 171744, https://doi.org/10.1016/j.jmmm.2024.171744.
[4] Č. Jovalekić, M. Zdujić, A. Radaković, M. Mitrić, Mechanochemical synthesis of NiFe2O4 ferrite, Mater. Lett. 24 (1995) 365–368, https://doi.org/10.1016/0167-577X(95)00120-4.
[5] P.A. Shaikh, R.C. Kambale, A.V. Rao, Y.D. Kolekar, Effect of Ni doping on structural and magnetic properties of Co1–xNixFe1.9Mn0.1O4, J. Magn. Magn Mater. 322 (2010) 718–726, https://doi.org/10.1016/j.jmmm.2009.10.048.
[6] A. Nikzad, R. Parvizi, Gh Rezaei, B. Vaseghi, R. Khordad, Structural, magnetic and microwave properties of nanocrystalline Ni-Co-Gd ferrites, J. Electron. Mater. 47 (2018) 1302–1310, https://doi.org/10.1007/s11664-017-5921-y.
[7] T. Tatarchuk, M. Myslin, I. Mironyuk, M. Bououdina, A.T. Pędziwiatr, R. Gargula, B. Bogacz, P. Kurzydło, Synthesis, morphology, crystallite size and adsorption properties of nanostructured Mg–Zn ferrites with enhanced porous structure, J. Alloys Compd. 819 (2020) 152945, https://doi.org/10.1016/j.jallcom.2019.152945.
[8] R. Ali, M.A. Khan, A. Mahmood, A.H. Chughtai, A. Sultan, M. Shahid, M. Ishaq, M. F. Warsi, Structural, magnetic and dielectric behavior of Mg1-xCaxNiyFe2-yO4 nano-ferrites synthesized by the micro-emulsion method, Ceram. Int. 40 (2014) 3841–3846, https://doi.org/10.1016/j.ceramint.2013.08.024.
[9] N. Millot, S. Le Gallet, D. Aymes, F. Bernard, Y. Grin, Spark plasma sintering of cobalt ferrite nanopowders prepared by coprecipitation and hydrothermal synthesis, J. Eur. Ceram. Soc. 27 (2007) 921–926, https://doi.org/10.1016/j.jeurceramsoc.2006.04.141.
[10] S. Sur, P.K. Tyagi, Sh Kr Jha, Flash sintering improves magnetic properties of spinel zinc ferrite, Scr. Mater. 236 (2023) 115681, https://doi.org/10.1016/j.scriptamat.2023.115681.
[11] Preeti Thakur, Neetu Gahlawat, Pinki Punia, Saarthak Kharbanda, Blaise Ravelo, Atul Thakur, Cobalt nanoferrites: a review on synthesis, characterization, and applications, J. Supercond. Nov. Magnetism 35 (2022) 2639–2669, https://doi.org/10.1007/s10948-022-06334-1.
[12] U. Jinendra, J. Kumar, B.M. Nagabhushana, A.V. Raghu, D. Bilehal, Facile synthesis of $CoFe_2O_4$ nanoparticles and application in removal of malachite green dye, Green Mater. 7 (3) (2019) 137–142, https://doi.org/10.1680/jgrma.18.00054.
[13] S. Choudhary, A. Bisht, S. Mohapatra, Facile synthesis, morphological, structural, photocatalytic and optical properties of $CoFe_2O_4$ nanostructures, SN Appl. Sci. 1 (2019) 1613, https://doi.org/10.1007/s42452-019-1665-z.
[14] F. Jelokhani, S. Sheibani, A. Ataie, Adsorption and photocatalytic characteristics of cobalt ferrite-reduced graphene oxide and cobalt ferrite-carbon nanotube nanocomposites, J. Photochem. Photobiol. Chem. 403 (2020) 112867, https://doi.org/10.1016/j.jphotochem.2020.112867.
[15] V. Crocellà, F. Cavani, G. Cerrato, S. Cocchi, M. Comito, G. Magnacca, C. Morterra, On the role of morphology of $CoFe_2O_4$ spinel in methanol anaerobic oxidation, J. Phys. Chem. C 116 (2012) 14998–15009, https://doi.org/10.1021/jp304355d.
[16] Jitendra Pal Singh, Jae Yeon Park, Varsha Singh, So Hee Kim, Weon Cheol Lim, Hemaunt Kumar, Y.H. Kim, Sangsul Lee, Keun Hwa Chae, Correlating the size and cation inversion factor in context of magnetic and optical behavior of $CoFe_2O_4$ nanoparticles, RSC Adv. 10 (2020) 21259–21269, https://doi.org/10.1039/D0RA01653E.
[17] J. Venturini, A. Mallmann Tonelli, T. Bender Wermuth, R. Young Sun Zampiva, S. Arcaro, A. Da Cas Viegas, C. Pérez Bergmann, Excess of cations in the sol-gel synthesis of cobalt ferrite ($CoFe_2O_4$): a pathway to switching the inversion degree of spinels, J. Magn. Magn Mater. 482 (2019) 1–8, https://doi.org/10.1016/j.jmmm.2019.03.057.
[18] T. Tatarchuk, A. Shyichuk, V. Kotsyubynsky, N. Danyliuk, Catalytically active cobalt ferrites synthesized using plant extracts: insights into structural, optical, and catalytic properties, Ceram. Int. 51 (2025) 4988–4999, https://doi.org/10.1016/j.ceramint.2024.11.470.
[19] P. Chandramohan, M.P. Srinivasan, S. Velmurugan, S.V. Narasimhan, Cation distribution and particle size effect on Raman spectrum of $CoFe_2O_4$, J. Solid State Chem. 184 (2011) 89–96, https://doi.org/10.1016/j.jssc.2010.10.019.
[20] H. Hussein, S.S. Ibrahim, Sherif A. Khairy, Biosynthesis of $CoFe_2O_4$ ferrite nanoparticles using Greek yogurt solution: deep structural insights and appraisal for ecological mitigation via quartz crystal microbalance, J. Water Proc. Eng. 65 (2024) 105856, https://doi.org/10.1016/j.jwpe.2024.105856.
[21] V. Bilovol, M. Sikora, S. Lisníková, J. Żukrowski, K. Berent, M. Gajewska, Occupancies of tetra- and octahedral sites in $CoFe_2O_4$ nanoparticles: the effect of the sintering temperature, J. Appl. Phys. 134 (2023) 094304, https://doi.org/10.1063/5.0163166.
[22] J. Mohapatra, M. Xing, J. Elkins, J. Beatty, J. Ping Liu, Size-dependent magnetic hardening in $CoFe_2O_4$ nanoparticles: effects of surface spin canting, J. Phys. Appl. Phys. 53 (2020) 504004, https://doi.org/10.1088/1361-6463/abb622.
[23] N. Daffé, F. Choueikani, S. Neveu, M.-A. Ario, A. Juhin, P. Ohresser, V. Dipuis, P. Sainctavit, J. Magn. Magn Mater. 460 (2018) 243–252, https://doi.org/10.1016/j.jmmm.2018.03.041.
[24] F.D. Saccone, S. Ferrari, D. Errandonea, F. Grinblat, V. Bilovol, S. Agouram, Cobalt ferrite nanoparticles under high pressure, J. Appl. Phys. 118 (2015) 075903, https://doi.org/10.1063/1.4928856.
[25] Z.Ž. Lazarević, Č. Jovalekić, A. Milutinović, D. Sekulić, V.N. Ivanovski, A. Rečnik, B. Cekić, N.Ž. Romčević, Nanodimensional spinel $NiFe_2O_4$ and $ZnFe_2O_4$ ferrites prepared by soft mechanochemical synthesis, J. Appl. Phys. 113 (2013) 187221, https://doi.org/10.1063/1.4801962.
[26] D. Tuschel, Stress, strain, and Raman spectroscopy, Spectroscopy 34 (9) (2019) 1–9. ISSN: 0887-6703 Online ISSN: 1939-1900.
[27] Jonathan E. Spanier, Richard D. Robinson, Feng Zhang, Siu-Wai Chan, Irving P. Herman, Size-dependent properties of CeO_2 nanoparticles as studied by Raman scattering, Phys. Rev. B (2001) 64245407, https://doi.org/10.1103/PhysRevB.64.245407.
[28] F.J. Manjón, D. Errandonea, J. López-Solano, P. Rodríguez-Hernández, A. Muñoz, Negative pressures in $CaWO_4$ nanocrystals, J. Appl. Phys. 105 (2009) 094321, https://doi.org/10.1063/1.3116727.
[29] D. Errandonea, F.J. Manjón, On the ferroelastic nature of the scheelite-to-fergusonite phase transition in orthotungstates and orthomolybdates, Mater. Res. Bull. 44 (2009) 807–811, https://doi.org/10.1016/j.materresbull.2008.09.024.
[30] Budi Purnama, Agung Tri Wijayanta, Suharyana, Effect of calcination temperature on structural and magnetic properties in cobalt ferrite nano particles, J. King Saud Univ. Sci. 31 (2019) 956–960, https://doi.org/10.1016/j.jksus.2018.07.019.
[31] Zhongwu Wang, R. Downs, Vittoria Pischedda, R. Shetty, Surendra Saxena, Chang-Sheng Zha, Y.S. Zhao, D. Schiferl, A. Waskowska, High-pressure X-ray diffraction and Raman spectroscopic studies of the tetragonal spinel $CoFe_2O_4$, Phys. Rev. B 68 (2003) 094101, https://doi.org/10.1103/PhysRevB.68.094101.
[32] P. Chandramohan, M.P. Srinivasan, S. Velmurugan, S.V. Narasimhan, Cation distribution and particle size effect on Raman spectrum of $CoFe_2O_4$, J. Solid State Chem. 184 (2011) 89, https://doi.org/10.1016/j.jssc.2010.10.019.
[33] Zorica Ž. Lazarević, Aleksandra Milutinović, Ljubica Andjelković, Milica Petrović, Branka Hadžić, Maja Romčević, Jelena Trajić, Nebojša Ž. Romčević, Characterization of cobalt ferrite nanoparticles obtained by various synthesis methods and comparison with the Raman spectra of other ferrites and some cubic oxide spinels, Sci. Sinter. (2023), https://doi.org/10.2298/SOS230322035L.
[34] Luis I. Granone, Anna C. Ulpe, Lars Robben, Stephen Klimke, Moritz Jahns, Renz Franz, Thorsten M. Gesing, Thomas Bredow, Ralf Dillert, Detlef W. Bahnemann, Effect of the degree of inversion on optical properties of spinel $ZnFe_2O_4$, Phys. Chem. Chem. Phys. 20 (2018) 28267, https://doi.org/10.1039/C8CP05061A.
[35] V.G. Hadjiev, M.N. Iliev, I.V. Vergilov, The Raman spectra of Co3O4, J. Phys. C Solid State Phys. 21 (1988) L199–L201, https://doi.org/10.1088/0022-3719/21/7/007.
[36] Martín Testa-Anta, Miguel A. Ramos-Docampo, Miguel Comesaña-Hermo, Beatriz Rivas-Murias, Verónica Salgueiriño, Raman spectroscopy to unravel the magnetic properties of iron oxide nanocrystals for bio-related applications, Nanoscale Adv. 1 (2019) 2086, https://doi.org/10.1039/C9NA00064J.
[37] Nahed Makram Eyssa, Hanan Hassan Hantour*, Kamilia Sdeek Abdo, Phase Formation and crystallinity-dependent magnetic parameters of $Co_{1-x}Fe_{2+x}O_4$ nanoparticals, Am. J. Phys. Appl. 3 (2) (2015) 33–38, https://doi.org/10.11648/j.ajpa.20150302.14.
[38] A.V. Ravindra, M. Chandrika, Ch Rajesh, Pratap Kollu, Shaohua Ju, S.D. Ramarao, Simple synthesis, structural and optical properties of cobalt ferrite nanoparticles, Eur. Phys. J. Plus 134 (2019) 296, https://doi.org/10.1140/epjp/i2019-12690-2.
[39] Tahani Saad Almutairi, Unraveling the complex interplay of phase transitionsin spinel ferrites:A comprehensive quantum mechanical vibrational study of ZnFe2O4, ACS Omega 8 (2023) 36999–37010, https://doi.org/10.1021/acsomega.3c04268.
[40] M. Andrés-Vergés, C. de Julián, J.M. González, C.J. Serna, Preparation and magnetic properties of monodispersed Zn ferrites of submicrometric size, J. Mater. Sci. 28 (1993) 2962–2966, https://doi.org/10.1007/BF00354700.
[41] Rohit R. Powar, Varsha D. Phadtare, Vinayak G. Parale, Sachin Pathak, Pravina B. Piste, Dnyandevo N. Zambare, J. Korean Ceram. Soc. 56 (5) (2019) 474–482, https://doi.org/10.4191/kcers.2019.56.5.06.
[42] Raghvendra Singh Yadav, Jaromir Havlica, Jiri Masilko, Lukas Kalina, Jaromir Wasserbauer, Miroslava Hajduchova, Vojtech Enev, Ivo Kritka, Zuzana Kozakova, Cation migration-induced crystal phase transformation in copper ferrite nanoparticles and their magnetic property, J. Supercond. Nov. Magnetism 29 (2016) 759–769, https://doi.org/10.1007/s10948-015-3339-4.
[43] Ł. Mazur, D. Koszelow, M. Zajusz, M. Łapiński, M. Bik, P. Zając, A. Adamczyk, P. Rutkowski, S. Molin, T. Brylewski, Comparison of $Cu_{1.3}Mn_{1.7}O_4$ spinels doped with Ni or Fe and synthesized via wet chemistry and solid-state reaction methods,

designed as potential coating materials for metallic interconnects, J. Eur. Ceram. Soc. 43 (2023) 5557–5574, https://doi.org/10.1016/j.jeurceramsoc.2023.05.015.
[44] K. Lankauf, K. Górnicka, P. Błaszczak, J. Karczewski, J. Ryl, G. Cempura, M. Zając, M. Bik, M. Sitarz, P. Jasiński, S. Molin, Tuning of e_g electron occupancy of $MnCo_2O_4$ spinel for oxygen evolution reaction by partial substitution of Co by Fe at octahedral sites, Int. J. Hydrogen Energy 48 (2023) 8854e8866, https://doi.org/10.1016/j.ijhydene.2022.12.013.
[45] N. Liu, P. Du, P. Zhou, R.G. Tanguruti, Y. Qi, T. Zhang, Ch Zhuang, Annealing temperaturę effects on the cation distribution in $CoFe_2O_4$ nanofibers, Appl. Surf. Sci. 532 (2020) 147440, https://doi.org/10.1016/j.apsusc.2020.147440.
[46] M.C. Biesinger, Accessing the robustness of adventitious carbon for charge referencing (correction) purposes in XPS analysis: insights from a multi-user facility data review, Appl. Surf. Sci. 597 (2022), https://doi.org/10.1016/j.apsusc.2022.153681.
[47] P.G. Rouxhet, M.J. Genet, XPS analysis of bio-organic systems, Surf. Interface Anal. 43 (2011), https://doi.org/10.1002/sia.3831.
[48] High Resolution XPS of Organic Polymers: The Scienta ESCA300 Database, G. Beamson, D. Briggs, J. Chem. Educ. 70 (5) (1993), https://doi.org/10.1021/ed070pa25.
[49] A.V. Naumkin, A. Kraut-Vass, C.J. Powell, S.W. Gaarenstroom, NIST Standard Reference Database 20 Version 4.1, The National Institute of Standards and Technology NIST, 2012.
[50] M.C. Biesinger, B.P. Payne, A.P. Grosvenor, L.W.M. Lau, A.R. Gerson, R.S.C. Smart, Resolving surface chemical states in XPS analysis of first row transition metals, oxides and hydroxides: Cr, Mn, Fe, Co and Ni, Appl. Surf. Sci. 257 (2011), https://doi.org/10.1016/j.apsusc.2010.10.051.
[51] A.P. Grosvenor, B.A. Kobe, M.C. Biesinger, N.S. McIntyre, Investigation of multiplet splitting of Fe 2p XPS spectra and bonding in iron compounds, Surf. Interface Anal. 36 (2004), https://doi.org/10.1002/sia.1984.
[52] Y. Lykhach, S. Piccinin, T. Skála, M. Bertram, N. Tsud, O. Brummel, M. Farnesi Camellone, K. Beranová, A. Neitzel, S. Fabris, K.C. Prince, V. Matolín, J. Libuda, Quantitative analysis of the oxidation state of cobalt oxides by resonant photoemission spectroscopy, J. Phys. Chem. Lett. 10 (2019), https://doi.org/10.1021/acs.jpclett.9b02398.
[53] Alka B. Garg, D. Vie, P. Rodriguez-Hernandez, A. Muñoz, A. Segura, D. Errandonea, Accurate determination of the band gap energy of the rare-earth niobate series, J. Phys. Chem. Lett. 14 (2023) 1762–1768, https://doi.org/10.1021/acs.jpclett.3c00020.
[54] A. Kalam, A.G. Al-Sehemi, M. Assiri, G. Du, T. Ahmad, I. Ahmad, M. Pannipara, Modified solvothermal synthesis of cobalt ferrite ($CoFe_2O_4$) magnetic nanoparticles photocatalysts for degradation of methylene blue with H_2O_2/visible light, Results Phys. 8 (2018) 1046, https://doi.org/10.1016/j.rinp.2018.01.045.
[55] A.V. Ravindra, P. Padhan, W. Prellier, Electronic structure and optical band gap of $CoFe_2O_4$ thin films, Appl. Phys. Lett. 101 (2012) 161902, https://doi.org/10.1063/1.4759001.
[56] P. Annie Vinosha, S. Jerome Das, Investigation on the role of pH for the structural, optical and magnetic properties of cobalt ferrite nanoparticles and its effect on the photo-fenton activity, Mater. Today Proc. 5 (2018) 8662–8671, https://doi.org/10.1016/j.matpr.2017.12.291.
[57] M. Srinivas, Preparation, characterization and photocatalytic activity of nickel-substituted $CoFe_2O_4$: exploration of changes in the micro structural parameters and distribution of cations in the lattice, Mater. Res. Express 6 (2019) 1150f9, https://doi.org/10.1088/2053-1591/ab51af.
[58] D. Sharma, N. Khare, Tuning of optical bandgap and magnetization of $CoFe_2O_4$ thin films, Appl. Phys. Lett. 105 (2014) 032404, https://doi.org/10.1063/1.4890863.
[59] B.S. Holinsworth, D. Mazumdar, H. Sims, Q.-C. Sun, M.K. Yurtisigi, S.K. Sarker, A. Gupta, W.H. Butler, J.L. Musfeldt, Chemical tuning of the optical band gap in spinel ferrites: $CoFe_2O4$ vs $NiFe_2O_4$, Appl. Phys. Lett. 103 (2013) 082406, https://doi.org/10.1063/1.4818315.